Objective Method for Measuring Tropical Cyclone Roll Vortices Using WSR-88D Radar Observations

James A. Schiavone *

Posted Date: 22 October 2025

doi: 10.20944/preprints202510.1610.v1

Keywords: tropical cyclones; hurricanes; boundary layer; roll vortices; landfall; extratropical transition

Article

Objective Method for Measuring Tropical Cyclone Roll Vortices Using WSR-88D Radar Observations

James A. Schiavone

Independent Researcher, Bridgewater, NJ 08807, USA; jimschiavone@gmail.com

Abstract

Roll vortices often occur in the tropical cyclone boundary layer and have been shown to enhance vertical momentum transport and to amplify surface winds at kilometer scale or lower. Thus, it is important to characterize the presence and intensity of such rolls in as many structural, life cycle and situational characteristics as possible. To aid that characterization, an objective method was developed to measure the presence and intensity of boundary layer roll vortices in tropical cyclones using operational WSR-88D radar observations. The method was developed using observations for landfalling Post-tropical Cyclone Sandy and entails interpolating WSR-88D radar radial velocity data to storm-centered radials. The radar velocity data are then segmented into 60-point samples to which a spectral analysis is applied to each sample. The maximum spectral variance of each sample is used as the metric for roll vortex intensity and a criterion was developed to discriminate roll presence based on the dominance of the spectral peak. Results are used to analyze the dependence of roll presence, intensity and wavelength on location, time, and terrain characteristics and to compare the results with those reported by others.

Keywords: tropical cyclones; hurricanes; boundary layer; roll vortices; landfall; extratropical transition

1. Introduction

Boundary layer roll vortices are vertically overturning circulations which have their rotation axes parallel to the ground and which are elongated along the prevailing wind vector. They were originally observed and characterized in airmass boundary layers [1–6] but later reported and studied in tropical cyclone (TC) boundary layers [7–15] and even in extratropical cyclones [16]. Roll vortices in TC boundary layers have been found to amplify surface wind speeds when and where they occur [7–10,13]. They also are suspected to contribute to TC intensity modulation [17] via enhanced vertical transport of momentum, a contribution which is not currently incorporated in TC boundary layer parameterizations in numerical weather prediction models [9,10,14,18–21]. Therefore, it is important to characterize their presence and intensity within a TC as well as among a broad a variety of TCs.

Theoretical studies [22,23] and numerical simulation analyses [24–30] have proposed mechanisms for the development, size and intensity of tropical cyclone roll vortices. These studies have shown that roll vortices are caused by an inflection point instability in the radial velocity profile within the boundary layer of a TC. Various instruments have been used to observe TC boundary layer roll vortices: satellite synthetic aperture radar (SAR) [13,31–33], aircraft [8,12,14], portable Doppler radars and lidars [7,11], and operational Doppler radars [8–10,15]. Operational Doppler radar systems are unique in that they have the ability to routinely measure wind speed fields within a large collection of TCs using an instrument that is mostly invariant among its many installations. Thus, this work leverages those benefits of the WSR-88D Doppler radar network of the United States National Weather Service [34] to develop an objective methodology to quantify the presence and intensity of roll vortices in TC boundary layers. The method is herein developed and tested for Post-tropical Cyclone Sandy (2012), with the intension of applying it to other TCs in future work to compile a climatology of roll vortex characteristics. Because of Post-tropical Cyclone (Post-TC) Sandy's

 doi:10.20944/preprints202510.1610.v1

catastrophic impacts on a large metropolitan area [35,36], its unusual trajectory [37,38], and its extratropical transition just before landfall [39,40], it has been the subject of many observational [15,41,42] and numerical simulation [38–40,43,44] studies and, thus, is a key opportunity to characterize TC roll vortices.

The work described herein builds upon earlier work [45] and develops a roll intensity metric that measures the periodicity of the rolls using spectral analysis of the radar radial velocity samples that lie along storm-centered radials. Section 2 describes the data used to develop the methodology, the steps used in the methodology, and its verification. Section 3 applies the technique to Post-TC Sandy to characterize numerous aspects of rolls observed during Post-TC Sandy's landfall, Section 4 compares results to those of others and Section 5 summarizes key results.

2. Data and Methods

2.1. Data

Doppler radar data [34] is from the WSR-88D radar station located at Fort Dix, NJ. The center of Post-TC Sandy traversed southern New Jersey in a west-northwestward direction about 50 km south of the radar site [46]. Full volume radar scans are produced approximately every 6 minutes, with a minimum elevation angle of 0.5 degree. Elevation angle resolution was only 1° during landfall, so only the lowest elevation angle of 0.5 degrees was practical to use for this analysis. Radial velocity data were used, for which range resolution is 0.25 km and azimuthal resolution is 1 degree. Doppler radar measures the motion of precipitation particles in the direction of the radar beam. Hereafter we refer to the velocity observed by Doppler radar as radar radial velocity, which should be distinguished from the radial velocity of the TC relative to its storm center. The specific base velocity data used for analysis is hourly for 1501 UTC 29 October 2012 through 0301 UTC 30 October 2012.

Surface observations at 5-minute intervals for the Rutgers NJ Weather Network [48] also were used, which is hereafter referred to as the NJ Mesonet. Surface observations at hourly intervals for 2 oceanic stations of the NOAA National Data Buoy Center (NDBC) [48] network were also used: stations 44065 and 44025 which were 25 and 72 km east-southeast of Sandy Hook, NJ, respectively.

2.2. Methods

The methodology developed herein is based on currently known characteristics of roll vortices that occur in TC boundary layers. Roll vortices, being helical circulations having rotation axes parallel to the ground and to each other, have been consistently observed to have their rotation axes aligned within a few degrees of the TC's tangential velocity [9–11,13], as illustrated in Figure 1a, reproduced here from [15], where the diagonal black arrow represents a radial pointing away from the storm center. Adjacent rolls rotate in opposite directions, producing alternating lines of updrafts and downdrafts. The downdraft lines transport horizontal momentum downward from the high-speed jet that tops the TC boundary layer. The downdraft lines, in turn, yield lines of enhanced wind speed at the surface, which alternate with lines of diminished wind speed beneath the updraft lines.

 doi:10.20944/preprints202510.1610.v1

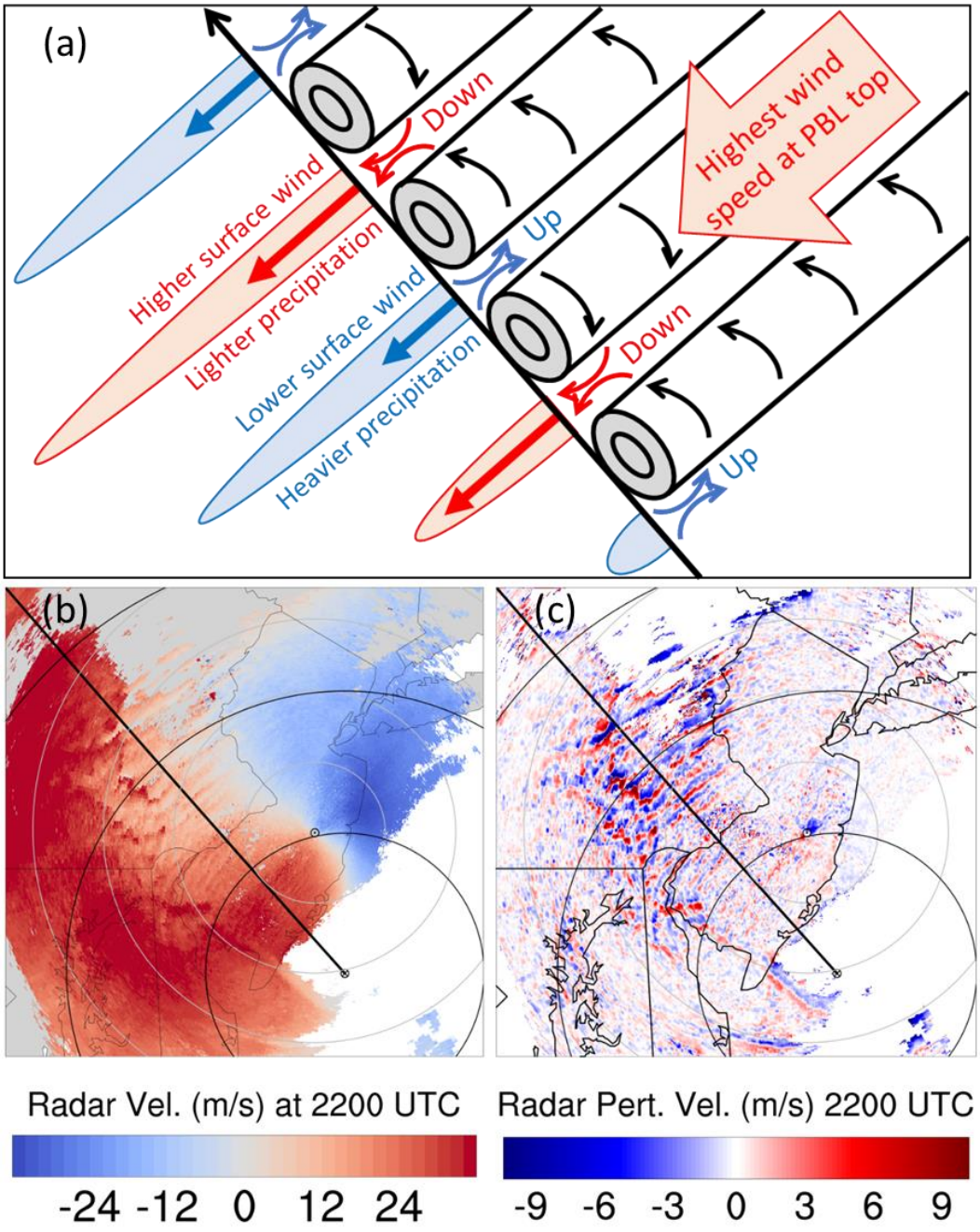

Figure 1. Roll vortex characteristics. (a) Conceptual depiction of roll vortices viewed from above, where the black diagonal arrow is an outward-pointing radial from the storm center. (b) Field of radar radial velocity, where blue and red are toward and away from the radar site, respectively, the black circled dot and × locate the radar site and storm center, respectively, large black circles denote incremental 100 km radii from the storm center, and large gray circles denote incremental 50 km radii from the radar site. (c) Field of perturbation radar velocity, where blue and red are below and above the background velocity, respectively.

These linear updraft-downdraft couplets are clearly visible in the example radar radial velocity (V_r) image shown in Figure 1b. The clarity of these features can be further improved by subtracting the smoothed, background, large-scale V_r field from the original radar velocity field, yielding the perturbation V_r field shown in Figure 1c. The large scale background V_r field was calculated by applying 100 iterations of a 9-point 2-dimensional smooth.

The method that was developed to quantify the presence and intensity of roll vortices in the boundary layer of tropical cyclones leverages the property that roll vortices exhibit periodic

 doi:10.20944/preprints202510.1610.v1

variations in V_r along storm-centered radials. The method details are described in the following steps and illustrated by the example shown in Figure 2.

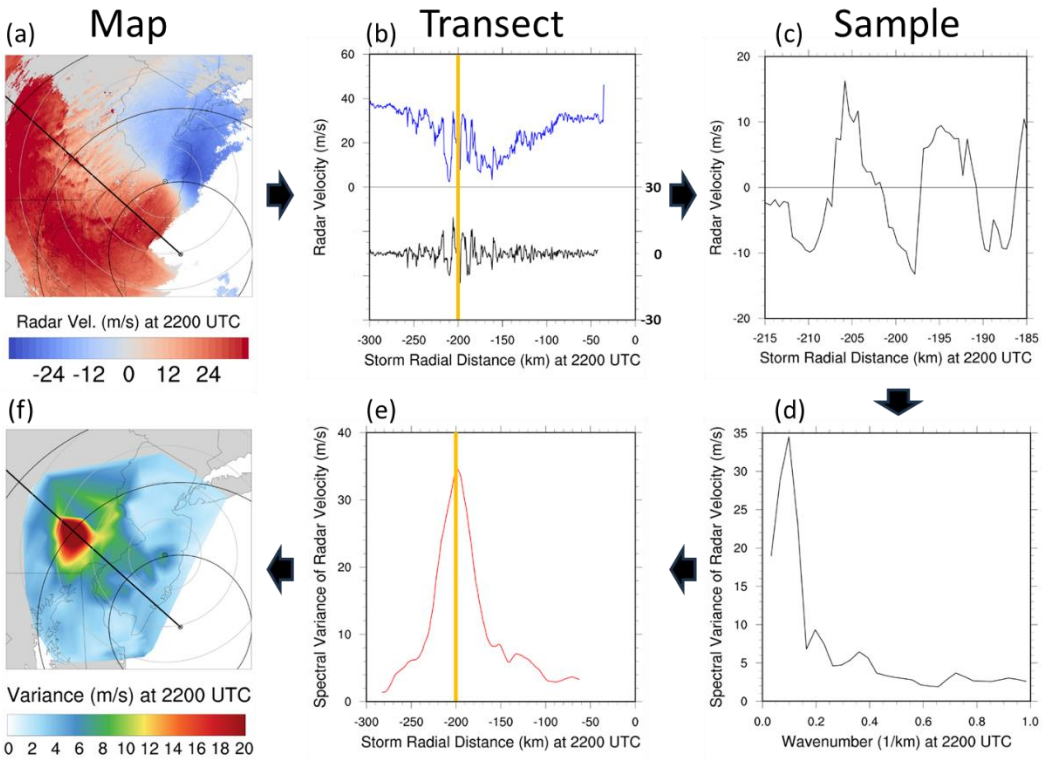

Figure 2. Example illustrating the roll intensity calculation method. (a) Field of radar radial velocity as in Figure 1b, where black diagonal line delineates storm-centered radial analyzed in this example. (b) Transect along black line in (a) of unfiltered and filtered radar radial velocity shown as blue and black plots, respectively, and where vertical yellow line denotes sample position analyzed in this example. (c) Filtered radar radial velocity series along 60-point sample denoted in (b) by yellow vertical line. (d) Spectral variance periodogram produced by spectral analysis of 60-point sample of filtered radar radial velocity. (e) Smoothed SV_{max} series calculated for all samples along example storm-centered radial. (f) Field of SV_{max} calculated for all samples along all storm-centered radials.

Step 1 involves reading the WSR-88D base velocity data into the NOAA Weather and Climate Toolkit (WCT) [49] and exporting it as an ESRI ASCII grid. Grid cell size is 0.005° latitude and longitude (≈ 0.5 km distance) for a domain of -77° to -73° longitude and 38.5° to 41.5° latitude, yielding 800×600 cells, respectively, of radar velocity data. An example velocity field is illustrated in Figure 2a for 2200 UTC 29 October 2012 where the circled dot and × locate the radar site and storm center, respectively. Blue and red shading indicate V_r toward and away from the radar site, respectively. Large black circles denote distance from the storm center at 100 km increments and large grey circles denote distance from the radar site at 50 km increments.

Step 2 involves interpolating the gridded radar radial velocity data onto storm-center-based radials. The gridded data is linearly interpolated onto 28 radials that span from the storm center to the farthest boundary of the analysis domain at 0.5 km increments on the storm radial. The far end points of the radials are at 0.5° latitude or longitude increments along the rectangular domain boundary. An example radial is shown as the black diagonal line on Figure 2a, with the interpolated radar velocity data for that radial shown as the blue plot in Figure 2b.

Step 3 establishes radar velocity data analysis samples along each storm radial at 0.5 km increments. The samples are 60 data points long, which corresponds to 30 km in radial length.

 doi:10.20944/preprints202510.1610.v1

Step 4 entails removing outlier values of radar velocity along each storm radial. This is accomplished by setting any individual radar radial velocity value that is more than 15 m/s beyond a 60-point sample average along the storm radial, to its 9-point-wide average along the radial. This is performed as a 60-point moving window analysis along the full length of each storm radial. About 0.5% of usable samples required this correction.

Step 5 applies a bandpass filter to admit roll wavelengths of 1-40 km along each storm radial, where a Lanczos sigma of 1 is used with 31 weight points. This wavelength range filters out wavelengths below the sampling resolution and above wavelengths of the largest known rolls. The filter was implemented using UCAR's NCAR Command Language (NCL) [50]. Figure 2c illustrates the radar velocity plotted for the sample identified as the yellow vertical line in Figure 2b at 200 km from the storm center.

Step 6 involves performing a spectral analysis along distance sequences of a storm radial sample, where the distance sequences are the 60 velocity data values as defined in step 3. In contrast to the more typical case of spectral analysis being applied to a temporal scale, in this case it is performed along a distance scale. The spectral analysis was implemented using the NCL [50] specx_anal function. The 60-point data samples were massaged by tapering 10% of the sample, removing the sample mean and its least squares linear trend, and applying 3-point periodogram smoothing. The spectral variance was computed for each frequency of the 30-point spectra representing the 60-point samples. Since units of spectral variance of radar radial velocity is $(m/s)^2$ and since this variable will be presented and discussed extensively in what follows, it is more informative to present the square root of spectral variance (SV) in all results hereafter so that they are in the more relatable velocity units of m/s. The resulting periodogram of SV as applied to the radar velocity of the sample shown in Figure 2c is shown in Figure 2d. Note that the maximum value of the spectral variance (SV_{max}) is at 0.1 km^{-1} wavenumber, which corresponds to a roll wavelength of 10 km.

Step 7 entails identifying the maximum value of SV for each analyzed sample. Given that the 30-point spectra correspond to 30 wavelengths spanning 0.5-30 km at 0.5 km intervals, it is assumed that the wavelength associated with SV_{max} is the dominant wavelength of the analyzed storm radial segment. SV_{max} is used as the metric of roll vortex intensity.

Step 8 entails smoothing the values of SV_{max} that were calculated for segment samples along storm radials by applying a 20-point running average (≈ 10 km distance) to the SV_{max} values along each storm radial. Figure 2e shows the result for the example radar radial velocity field shown in Figure 2a.

Steps 4-8 above are applied to all samples along each of the 28 radials that emanate from the storm center and extend to far ends that terminate at the rectangular analysis domain boundaries. The far end points are separated at the vertical and horizontal domain boundaries by increments of 0.5 degree in latitude and longitude, respectively. Figure 2f shows the resulting geographical distribution of SV_{max}.

To discriminate whether rolls are present, a criterion for the dominance of the SV_{max} spectral peak within each sample is established, above which rolls are assumed to be present. The ratio SV_{max}/SV_{med} is used as a measure of the dominance of the SV_{max} spectral peak among its 30 spectral members, where SV_{med} is the median SV of the spectral sample. A threshold value of $SV_{max}/SV_{med} \geq 3$ is used as the criterion for roll presence. The value of 3 was chosen by careful and comprehensive comparison of roll presence thus measured with visual detection of rolls in radar velocity and perturbation velocity imagery, such as imagery shown in Figures 3a-j. A key feature of this criterion is that it does not discriminate against shorter wavelength rolls, which usually have lower SV_{max} values.

 doi:10.20944/preprints202510.1610.v1

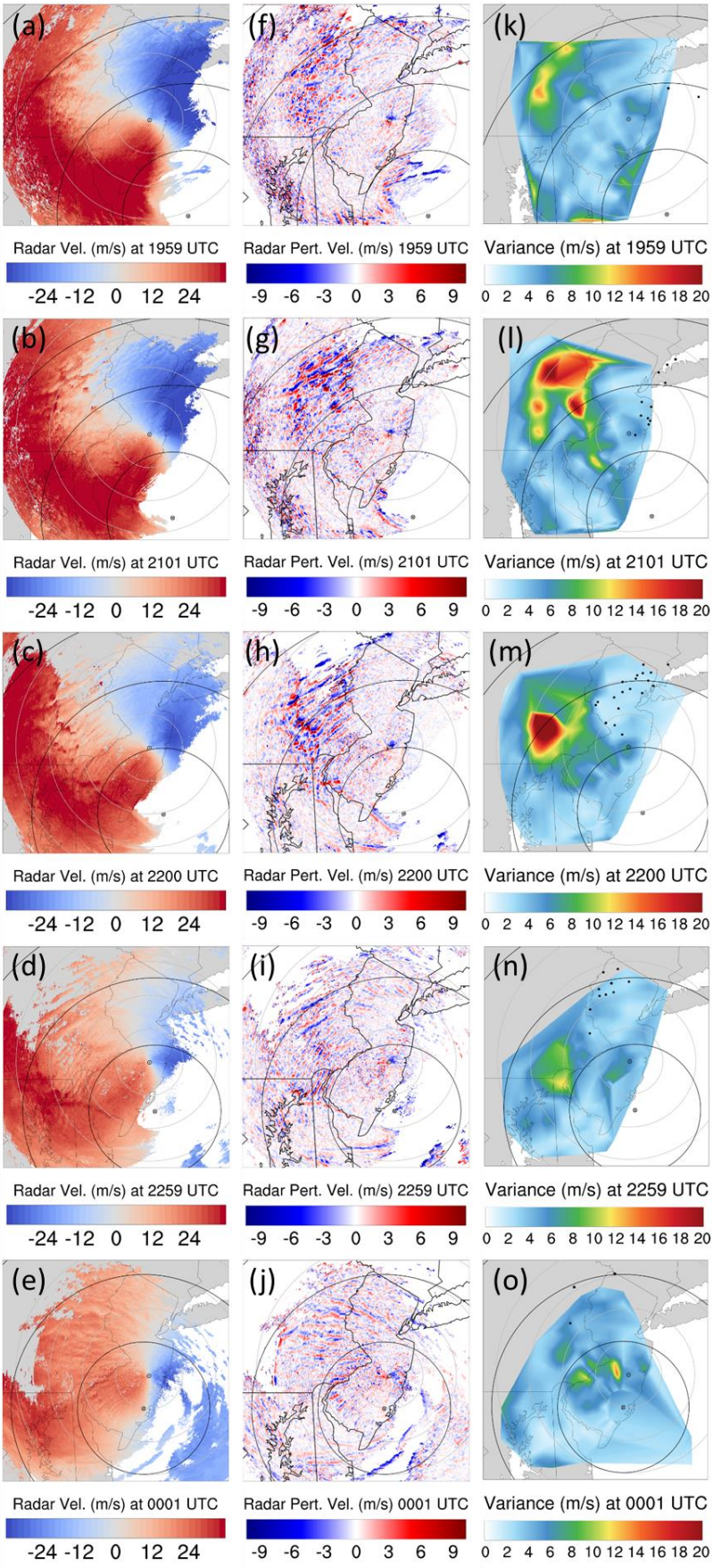

Figure 3. Spatial comparison of observed radar radial velocity and calculated roll vortex intensity metric. (a-e) Fields of radar radial velocity, as in Figure 1b, for 5 consecutive hours ending at landfall time. (f-j) Fields of

 doi:10.20944/preprints202510.1610.v1

perturbation radar velocity, as in Figure 1c, for same 5 hours. (k-o) Fields of SV_{max}, as in Figure 2f, for same 5 hours.

2.3. Metric Verification

A method was developed to map observed roll intensity using fields of the roll intensity metric that was calculated along 28 radials extending from the storm center. The method is verified by comparing map images of the original radar radial velocity with those of SV_{max} at each of 13 hours of data. Five hours of such comparisons are shown in Figure 3, wherein Figures 3a-e show the original radar radial velocity, Figures 3f-j show the perturbation V_r field, and Figures 3k-o show the computed SV_{max} field (scattered black dots locate certain weather stations which will be discussed in Section 3.2). By visual comparison of pairs of V_r and SV_{max} maps, it is quite evident that wherever rolls are evident on the V_r maps, elevated values of SV_{max} are present on those maps. Likewise, wherever there is no evidence of rolls on the V_r maps, very low values of SV_{max} are present on those maps.

3. Results

3.1. Roll Characterization Metrics

Besides SV_{max}, it is useful to quantify other measurements of roll vortex characteristics from the 60-point samples. Roll wavelength is specified as the wavelength corresponding to the wavenumber at which SV_{max} occurs within each sample. Measurement of the wind velocity variability attributed to rolls is also important. To this end, quantification of the maximum positive and negative departures from the average radar radial velocity of each sample are calculated. It should be emphasized, however, that because the velocities being analyzed are radar radial velocities and not necessarily aligned with the roll vortex axes, they represent a lower limit on the roll-attributed wind velocity fluctuations. A quantification of the impact of rolls on the likelihood of higher wind speeds is provided in Section 4.4. Histograms of several roll vortex metrics are shown in Figure 4.

Figure 4a shows the distribution of the spectral variance among all 60-point samples analyzed, which exhibits a lognormal behavior. Figure 4b shows the roll vortex wavelength distribution, which has a peak somewhere in the vicinity of 10 meters. The lack of specificity in the location of the wavelength peak is due to the limited resolution at low wavenumbers of the spectrum produced by the spectral analysis of the 60 sample points at distance increments of 0.5 km. Specifically, the comparatively large wavenumber increment at low wavenumbers corresponds to wavelengths calculable only at 7.6, 10.2 and 15.2 km, which is responsible for the sparsity of data between 7.6 and 15.2 km wavelengths. Thus, it is possible that the dominant wavelength is actually between 7.6 and 10.2 km since the samples included in the 10.2 km wavelength bar are likely accumulated from a range of wavelengths neighboring 10.2 km. Figure 4c shows the maximum positive and negative departures from the sample average radar radial velocity, where the solid and hatched blue bars represent positive and negative departures, respectively. Larger negative velocity departures are slightly more common than positive departures. Specifically, the average velocity amplitude is 5% larger for negative departures than positive departures. Finally, Figure 4d shows the distribution of the range (maximum minus minimum) of radial velocity observed among all 60-point radar samples along all storm radials, for which the average velocity range is 6.9 m/s.

 doi:10.20944/preprints202510.1610.v1

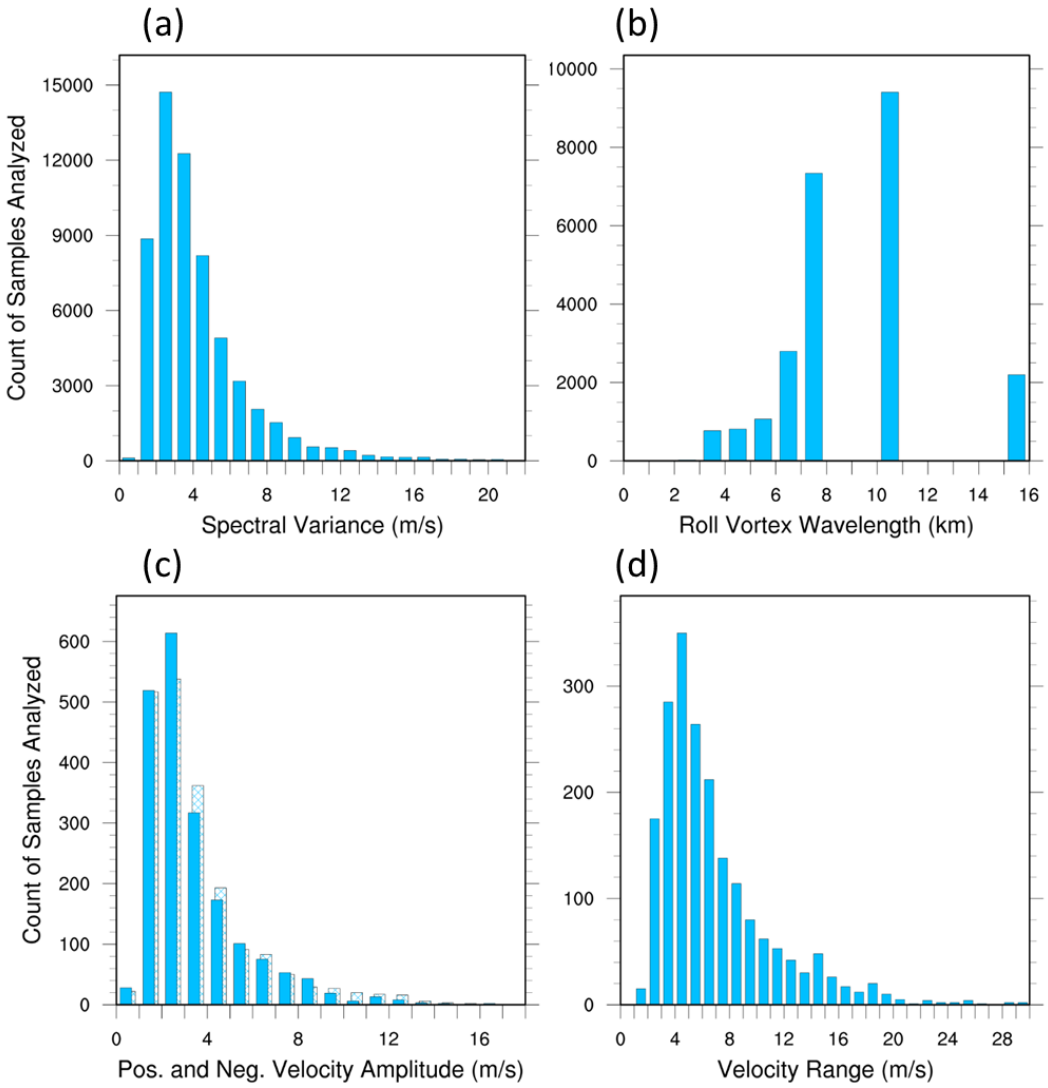

Figure 4. Roll metric histograms of analyzed radar radial velocity samples. (a) Maximum spectral variance of sample. (b) Wavelength at maximum spectral variance of sample. (c) Positive and negative maximum departures from each sample's mean radar radial velocity, where negative departures are shown as hatched. (d) Range of radar radial velocity, which is the maximum minus minimum velocity for each sample.

3.2. Reanalysis of Roll Association with Airstreams

We now apply the new roll intensity metric to a key topic of our prior work [45]: association of rolls with airstream type. In that prior work, we used the standard deviation of radar radial velocity observations that were enclosed within 0.2-degree latitude-longitude squares as a metric of roll intensity. We now use the new metric to reanalyze the association of rolls with storm airstream sectors. NJ Mesonet observations [47] recorded at 5-minute intervals and NDBC buoy observations [48] are used to identify whether the observation stations are in the warm sector. The airstream sector analysis method is similar to that of our prior work except that the method has been automated to objectively examine the temperature time series at each observation station. The maximum rate of temperature increase is used to identify the time of the surface warm front passage and the maximum temperature is used to identify the time of the leading edge of the surface seclusion's passage. The times of both airmass surface boundary passages are recorded for each station. Thus, the presence of each type of the 3 air masses, the pre-warm front cold conveyor belt (CCB), the warm sector, and the seclusion, can be assigned at each station at each time.

 doi:10.20944/preprints202510.1610.v1

As an illustration, Figures 5a and 5b show the arrival times of the warm sector and the seclusion, respectively, at each station north of 40.2 degrees latitude. The latter demarcates the minimum latitude at which sector delineation is possible. Figure 5 indicates that most stations are in the warm sector for about an hour as measured by the time difference between the two least-squares-fit lines at a given station longitude.

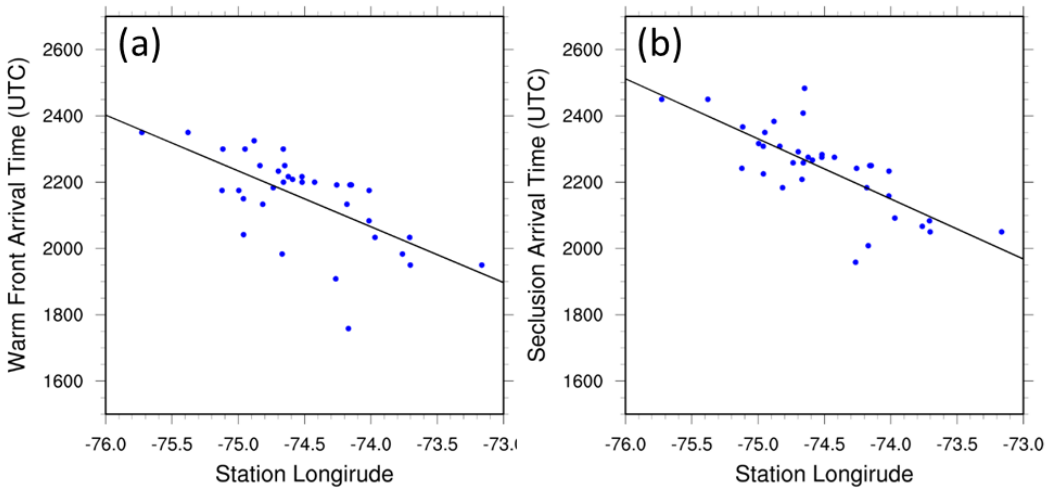

Figure 5. Arrival times of airstream sector surface boundaries at surface observation stations. (a) Surface warm front arrival time, where black line is a linear-least-squares fit to the observations. (b) Seclusion's forward surface boundary arrival time.

On the SV_{max} maps in Figures 3k-o, stations which are identified as being in the warm sector are plotted as black dots. Figures 3k-o show that the roll intensity metric, SV_{max}, is indeed low in the vicinity of stations that are in the warm sector. Knowing which airstream envelops any station at any time allows one to measure SV_{max} at each station and categorize it according to which of the 3 airmass types are present at that station. Results are show in Figure 6 as scatter and box plots. Despite the relative paucity of observations in the warm sector, as evident in Figure 6a, the median, average and quartile values of SV_{max} are much lower in the warm sector than in the neighboring sectors (Figure 6b), confirming the findings of our prior work that roll vortices are less prevalent or absent in the warm sector compared to the sectors preceding and following it.

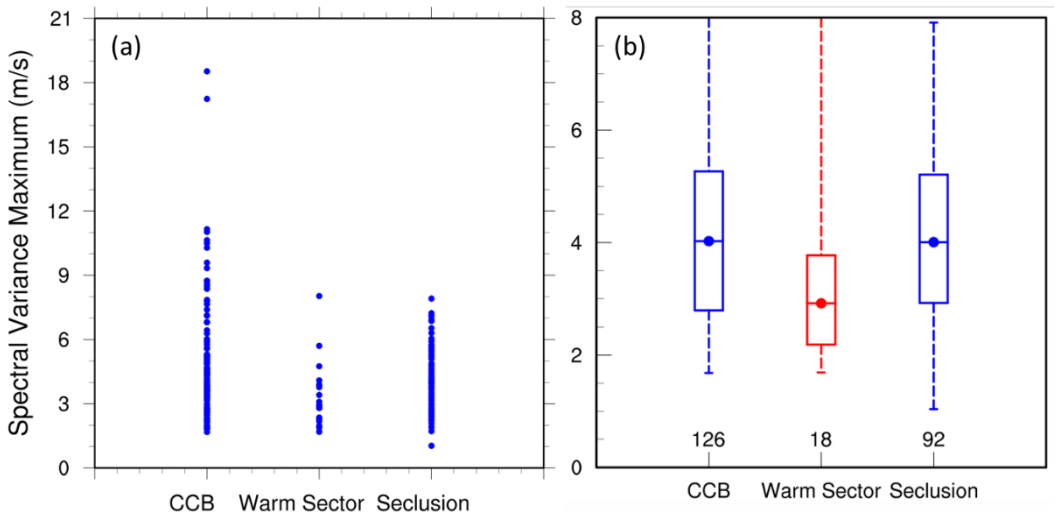

Figure 6. Roll intensity distribution among three airstream sectors. (a) Scatter plot of maximum spectral variance of each analyzed sample, categorized by the three airstream sectors. (b) Box plot of same data as (a), where dots,

 doi:10.20944/preprints202510.1610.v1

box limits and dashed-line limits represent means, quartiles and extremes, respectively, and numbers above X-axis are the number of samples classified in each airstream sector category.

3.3. Roll Variation with Location, Time and Terrain

We now characterize how the rolls vary with location relative to the storm center (distance and azimuth), time evolution during the landfall period and the underlying terrain relief and roughness length. Values of the roll intensity metric, SV_{max}, and roll wavelength are categorized according to 4 different ranges of distance and azimuth angle from the storm center, radar scan time, and terrain elevation and roughness length. Wavelengths are assigned as missing for data points at which rolls are deemed absent, as discussed at the end of Section 2.2 above. Then boxplots are produced which show the quartiles, median and mean for the distributions of roll intensity and roll wavelength for each of 4 ranges of the 5 dependent variables analyzed. Results are shown in Figures 7 and 8, where mean and median values are shown as red plus signs and blue dots, respectively, with the number of analyzed radar velocity samples listed at the bottom of each plot above its X axis.

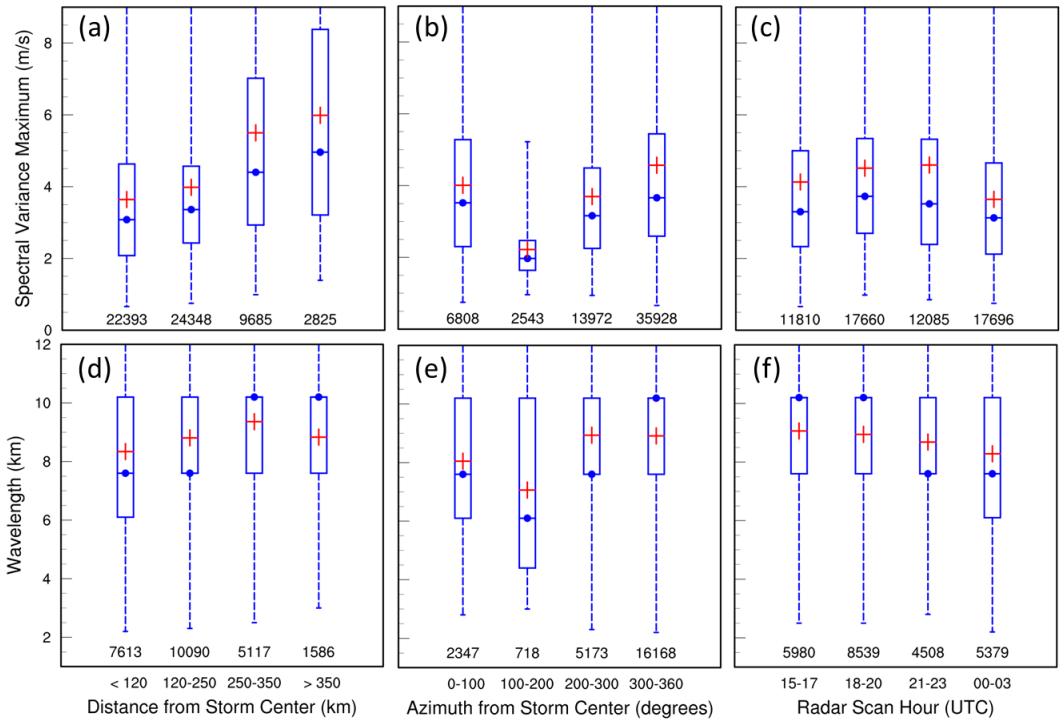

Figure 7. Roll intensity and wavelength distribution among four categories of distance and azimuth from storm center and time. (a-c) Maximum spectral variance of samples, where numbers above X-axis are the number of samples in each category. (d-f) Wavelength at maximum spectral variance.

 doi:10.20944/preprints202510.1610.v1

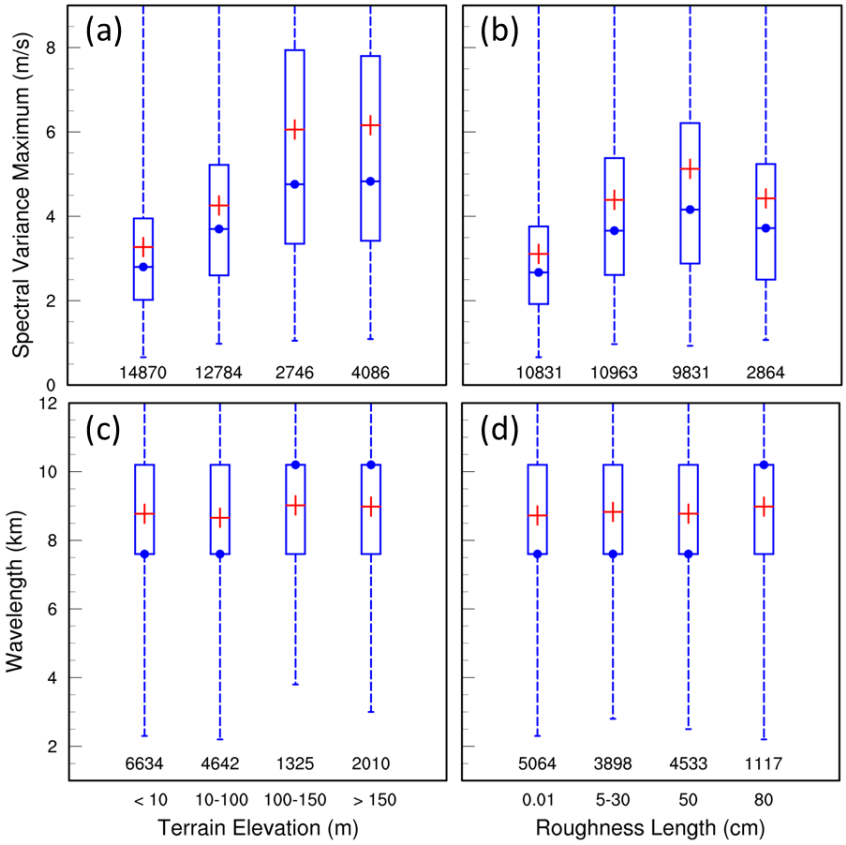

Figure 8. Roll intensity and wavelength distribution among four categories of terrain elevation and roughness length. (a-b) Maximum spectral variance of samples, where numbers above X-axis are the number of samples in each category. (c-d) Wavelength at maximum spectral variance.

Roll intensity increases with distance from the storm center (Figure 7a), with terrain elevation (Figure 8a), and with terrain roughness up to 50 cm (Figure 8b). Figure 8b also shows that roll intensity over land (roughness length > 0.01 cm) is higher than over water (roughness length = 0.01 cm). Figure 7b shows that roll intensity is low in the left rear storm quadrant (100-200° azimuth) and high in the right front quadrant (300-360° azimuth). Finally, roll intensity reaches its highest values during 1800-2000 UTC, about 5 hours before landfall (Figure 7c), and decreases thereafter.

Roll wavelength is mostly in the 6-10 km range, but wavelengths increase slightly with distance within 350 km of the storm center (Figure 7d). Wavelengths are shortest in the left rear storm quadrant (100-200° in Figure 7e) and decrease with time, especially after 2000 UTC (Figure 7f). Figures 8c,d show that roll wavelength varies little with terrain characteristics.

3.4. Roll Presence Analysis

We now analyze the presence of rolls as a function of the variables discussed above. To this end, the percentage of samples for which rolls are present is calculated as the percentage of analyzed samples for which $SV_{max}/SV_{med} \geq 3$, as discussed in Section 2.2. Recall that samples represent 60 half-kilometer increments along storm-centered radials for which precipitation is present, so the analyzed area varies hourly as the precipitation shield varies geographically. Results are shown in Figure 9 for the five same variables analyzed in Section 3.3.

 doi:10.20944/preprints202510.1610.v1

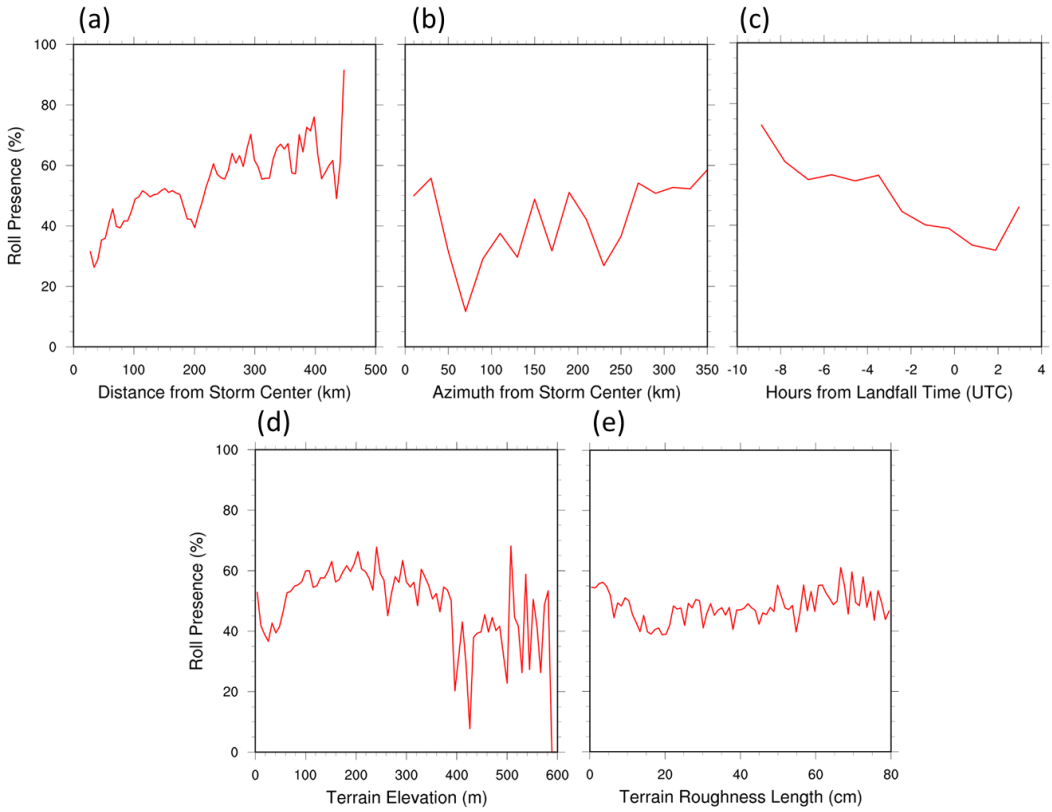

Figure 9. Roll presence percentages vs location, time and terrain characteristics. (a) Distance from storm center. (b) Azimuth from storm center, where north is 360°. (c) Hours from landfall time, where hour 0 is landfall time of 0000 UTC 30 October 2012. (d) Terrain elevation. (e) Terrain roughness length.

Figure 9a shows that their presence percentage generally increases from 30% to more than 60% with distance from the storm center, albeit with a plateau beyond 300 km distance. Figure 9b shows that roll presence is lowest in the right rear segment (12% at 70° azimuth) and highest in the forward segment (50-60% between 270° and 30° azimuth). Figure 9c shows that the percentage of the precipitation shield occupied by rolls declines significantly from above 70% to below 40% during the 13 hours studied, with an uptick during the last hour studied. Figure 9d shows that presence is higher (50-60%) for modest terrain elevation (60-400 km) but lower (~40%) for the lowest and highest elevations, although with sparser and noisy data at the highest elevations. Finally, Figure 9e shows that roll presence exhibits little systematic variation with terrain roughness length.

3.5. Wind Speed Enhancement Estimate

Previous work [15] demonstrated that more hazardous winds are more likely where rolls are present compared to absent. An analysis analogous to that performed earlier using surface wind speeds from the Weather Research and Forecasting (WRF) model is performed herein, except now using observed radar radial velocities. Probability distribution functions (PDFs) of the radar velocity normalized by its average along 30 km segments of its storm radial are shown in Figure 10a, where red and blue lines denote radar samples with and without rolls, respectively. Figure 10b, which plots the same pair of PDFs as Figure 10a on an exaggerated vertical scale, reveals that observations where rolls are present yield a higher likelihood of exceptionally high and low wind speeds.

 doi:10.20944/preprints202510.1610.v1

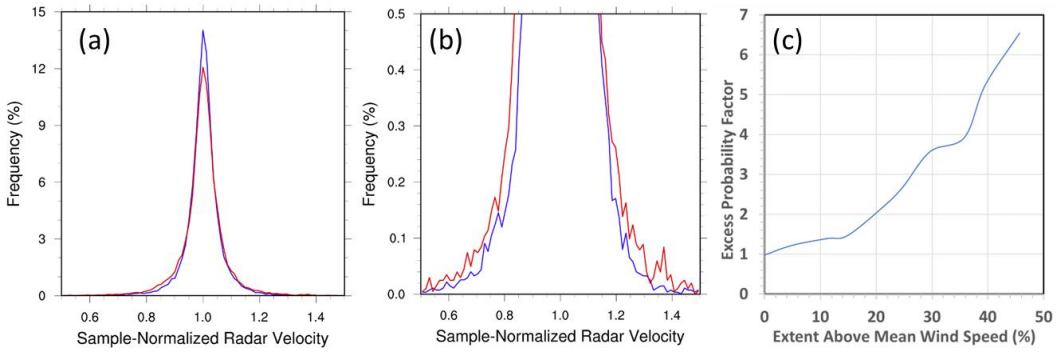

Figure 10. Estimation of excess likelihood of hazardous winds during roll vortex presence. (a) Probability density function of sample-normalized perturbation radar radial velocity. (b) Same probability density function with exaggerated vertical scale. (c) Excess probability factor for wind speed exceeding its mean wind speed for presence versus absence of roll vortices in such a storm.

This excess likelihood of more hazardous winds can be quantified by calculating the cumulative probability that wind speed exceeds a particular percentage above its mean wind speed and comparing those results for observations with and without rolls. Figure 10c shows the results of such an analysis, where the Y axis plots the ratio of a pair of cumulative probabilities, where the numerator and denominator are for samples with and without rolls present, respectively. This ratio is called the excess probability factor. For example, Figure 10c shows that it is 5.4 times more likely for wind speeds to exceed 40% above their mean speed when rolls are present.

4. Discussion

Others who have reported analyzing tropical cyclone roll vortices using operational WSR-88D radar data, which are most relevant for comparison with results reported herein, are Gall et al. [8] in the southeastern United Sates, Ellis and Businger [9] in Guam, Morrison et al. [10] in North Carolina and the Caribbean Sea, and Lorsolo et al. [11] in North Carolina and Florida. Gall et al. studied Hurricane Erin using WSR-88D data on 3 August 1995, Ellis and Businger [9] studied Typhoon Dale on 8 November 1996 and Typhoon Keith on 2 November 1997, Morrison et al. [10] studied Hurricane Georges in 1998, Hurricane Fran on 8 September 1996 and Hurricane Bonnie on 2 August, and Lorsolo et al. [11] studied Hurricane Isabel on 18 September 2003 and Hurricane Frances on 5 September 2004.

A key feature of the method used herein is that our analysis is automated and objective while those used by others are predominantly done manually. Another key feature of our method is that our analysis quantifies spectral intensity and periodicity of observed radar velocity variations along storm-centered radials and, thus, is able to measure not only the intensity of rolls where they are present, but also objectively discriminate where they are absent. Finally, multiple radar scan elevation angles were used by Ellis and Businger [9] and Morrison et al. [10], while ours was limited by radar elevation angle resolution and, thus, was restricted to the lowest elevation angle to ensure that the radar scan cone was in the boundary layer at our large distances from the radar site.

4.1. Roll Presence Comparisons

In the 13 hourly WSR-88D radar scans studied during Post-TC Sandy's landfall, rolls were observed in 42% of the radar radial velocity samples that fell within our fixed rectangular geographical domain. By comparison, Morrison et al. [10] observed that 35-69% of WSR-88D radar scans showed rolls after their initial presence, which brackets the results reported herein. Katsaros et al. [31] found that rolls are observed in all 4 storms that they studied, but they do not quantify a percentage coverage of rolls within those storms. Our roll occurrence over water is 47% compared to 40% over land, which is consistent with that which Ellis and Businger [9] observe, who note that more rolls occur over water than land.

 doi:10.20944/preprints202510.1610.v1

Figure 9a shows that roll presence increases from 30% to more than 60% with distance from the storm center, albeit with a plateau beyond 300 km distance, while Figure 9b shows that roll presence is lowest in the right rear segment (12% at 70° azimuth) and highest in the forward segment (50-60% between 270° and 30° azimuth). This spatial behavior relative to the storm center is consistent with the roll model predictions of Gao and Ginis [30]. Figure 9c shows that roll presence in the precipitation shield occupied by rolls declines significantly from above 70% to below 40% during the 13 hours studied, with an uptick during the last hour studied. This is consistent with our prior analysis of Sandy as illustrated by the green plot in Figure 4a of [15]. Roll presence and intensity variation with terrain characteristics (Figures 9d,e) are discussed jointly in Section 4.3 below.

4.2. Roll Wavelength Comparisons

We now compare the wavelength results reported herein with those reported previously. Since wavelengths are the most ubiquitously measured characteristic of TC roll vortices, a summary of published wavelength observations is provided in Table 1. Per our histograms in Figure 4b, our wavelengths of 3-15 km are similar to the wavelengths observed by Gall et al. [8], Katsaros et al. [31] and Foster [23], while larger than the wavelengths observed by the other reports listed in Table 1.

Table 1. Roll vortex wavelength observations.

Publication	Observation Method	Range (km)	Mean (km)
Wurman and Winslow, 1998 [7]	Mobile radar	–	~0.6
Gall et al., 1998 [8]	WSR-88D	–	~10
Katsaros et al., 2000 [31]	SAR	4-6	–
Morrison et al., 2005 [10]	WSR-88D	0.5-3.0	1.45
Foster, 2013 [13]	SAR	10-20	–
Reppucci et al., 2007 [33]	SAR	0.6-2.0	0.99
Lorsolo et al., 2008 [11]	WSR-88D	0.2-1.4	0.5
Zhang et al., 2008 [12]	Aircraft	–	0.9
Ellis and Businger, 2010 [9]	WSR-88D	0.4-2.8	1.35
Huang et al., 2018 [32]	SAR	0.6-1.6	–
Tang et al., 2021 [14]	Aircraft	0.3-3.0	–
Schiavone et al., 2021 [15]	WSR-88D	5-14	8.6
This work	WSR-88D	3-15	8.7

The wavelengths of rolls observed by Morrison et al. [10] are distributed lognormally. Because of the limited resolution of our wavelength measurements at smaller wavenumbers (longer wavelengths in Figure 4b), it cannot be confirmed whether the wavelengths reported herein are also distributed lognormally.

Figure 7d shows that wavelengths increase slightly with distance within 350 km of the storm center. This behavior can be explained by the roll model of Gao and Ginis [30], which predicts that wavelength is proportional to the boundary layer's shear layer depth (SLD), and WRF simulation results of Post-TC Sandy discussed by Schiavone et al. [15]. Figure 10 of [15] shows that SLD increases with distance from the storm center and, by implication of the roll model, so should roll wavelength. Figure 7f shows that wavelength decreases with time, especially after 2000 UTC. Per Schiavone et al. [15] in the green plot of their Figure 9a, SLD at the radar site decreases with time after 1900 UTC, and again, by implication of the roll model, so should roll wavelength. Figures 8c,d show that wavelength varies little with terrain characteristics. Per the same roll model, wavelength is proportional to the SLD of the boundary layer, so lack of influence of the lower physical surface boundary is not surprising.

Huang et al. [32] found that the observed maximum wavelength occurred at a distance from the storm center that is 1-2 times the radius of maximum wind (RMW) of the hurricane. From HURDAT2

 doi:10.20944/preprints202510.1610.v1

[51] and NJ Mesonet wind observations [47], the RMW at 1800 UTC 29 October 2012 for Post-TC Sandy is about 150 km. Figure 7d indicates that the longest wavelengths are 250-350 km from the storm center, indicating that the maximum wavelength occurred at distances from the storm center that are 1.7-2.3 times the RMW for Post-TC Sandy. This is on the high side of that reported by Huang et al. [32], but there is considerable uncertainty in the quantification of RMW for a storm that is undergoing extratropical transition during landfall and growing more asymmetric as time progresses. Huang et al. [32] also found that larger rolls are on the forward side of Hurricane Katrina, per their Figure 10. This is consistent with our results of Figure 7e, which show that the longest wavelengths for Post-TC Sandy occurred in the 200-360° azimuth range, which corresponds to the forward side of the west-northwestward moving storm.

4.3. Roll Intensity Comparisons

Figure 7a shows that roll intensity increases with distance from the storm center and Figure 7b shows that it is low in the left rear storm quadrant (100-200° azimuth) and high in the right front quadrant (300-360° azimuth). These observations on where roll growth is more intense is consistent with the roll model predictions of Gao and Ginis [30]. Figure 7c shows that roll intensity reaches its highest values during 1800-2000 UTC, about 5 hours before landfall and decreases thereafter. The time progression of roll intensity (Figure 7c) reflects the storm approaching and then decaying after 2000 UTC. Roll presence also diminishes faster after 2000 UTC. This temporal behavior is consistent with our prior analysis of Sandy [45] and is consistent with numerical studies of Gao and Ginis [30]. Roll intensity increases with terrain relief and roughness length up to 50 cm (Figure 8a-b). Roll presence is highest for moderate terrain relief of 60 to 400 m (Figure 9d) but shows little variation with terrain roughness length (Figure 9e). This suggests that terrain may have little effect on where rolls form, but that terrain relief and roughness may enhance their intensity where they do form.

Our mean radial velocity difference between positive and negative roll perturbations, among all roll samples, is 7 m/s (Figure 4d), which is lower than the values observed by Gall et al. [8] and Morrison et al. [10], who report values of 8 and 14 m/s, respectively. However, this is expected because Post-TC Sandy was already in its extratropical transition stage and weaker than the storms studied by the others.

Ellis and Businger [9] note that there is a slight asymmetry in the distribution of positive and negative extremes in velocity between adjacent roll peaks and troughs. Per the histogram in Figure 4c, our results show slightly higher populations for higher amplitudes of negative velocity compared to positive velocity, as do those of Ellis and Businger [9]. The latter reported averages of negative and positive velocity amplitudes of 7 and 6 m/s, respectively. Although our average negative and positive amplitudes are only slightly different at 3.5 and 3.3 m/s, respectively, they differ in the same direction as Ellis and Businger [9]. Foster's model [23] predicts that roll updrafts are stronger than their downdrafts, which would yield larger negative velocity perturbations than positive ones. Thus, Foster's predictions are supported by the two sets of observations described above.

5. Conclusions

A new roll intensity metric was developed which quantifies the periodic variability in observed WSR-88D radial wind velocity along storm-centered radials, where spectral variance is used to measure that periodic variability. The metric associates the wavelength of the maximum spectral variance within each 60-point sample segment as the wavelength of the rolls along that segment. The roll intensity and wavelength metrics are used to objectively analyze roll presence, intensity and wavelength as a function of numerous variables and to compare these results with those of others.

The new metric accurately represents the location and intensity of rolls during Post-TC Sandy's landfall. The roll metric shows that the roll intensity is higher in the cold conveyor belt and in the seclusion than in the warm sector, confirming the behavior reported previously [45]. Among all radar radial velocity samples analyzed over the 13 hours spanning landfall time, roll intensity, as measured by spectral variance of the samples, is highest at greatest distances from the storm center, in the

 doi:10.20944/preprints202510.1610.v1

forward sector of the storm, about 3 hours before landfall, at largest terrain relief values, and at higher terrain roughness lengths of 50 cm.

Roll wavelengths are largest at greater distances from the storm center, in the storm's forward sector, and earliest before landfall. Wavelength is essentially invariant with terrain, either relief or roughness length. The percentage of Post-TC Sandy's rain shield occupied by rolls increases with distance from the storm center and decreases with time through the landfall period. Roll presence percentage is highest for medium terrain relief and in the storm's forward sector, but exhibits little dependence on terrain roughness length.

Where comparisons are possible with observations and predictions of others, there is general agreement regarding where rolls occur and how their wavelengths vary relative to the storm center and its motion. Among the 11 prior reports of TC boundary layer roll wavelengths since 1998, the wavelengths of 3-15 km reported herein are comparable to 3 of the prior studies, although the majority of the others report shorter wavelength rolls. Future work will focus on applying the methodology developed herein to tropical cyclones beyond Post-TC Sandy for which WSR-88D radial velocity data is available, with the ultimate goal of compiling a climatology of tropical cyclone roll vortex characteristics.

Funding: This research received no external funding.

Data Availability Statement: Datasets for this research are available in these in-text data citation references: NOAA Radar Operations Center (1991) [34], Rutgers NJ Weather Network (2014) [47] and NOAA National Data Buoy Center (2016) [48].

Acknowledgments: The author is grateful to David A. Robinson and Mathieu R. Gerbush for providing data from the NJ Mesonet as well as for assistance in analyzing it and to Kun Gao for inspiring further studies of TC roll vortices.

Conflicts of Interest: The author declares no conflict of interest.

Abbreviations

The following abbreviations are used in this manuscript:

TC	Tropical cyclone
SAR	Synthetic aperture radar
NDBC	National Data Buoy Center
NOAA	National Oceanic and Atmospheric Administration
WCT	Weather and Climate Toolkit
ESRI	Environmental Systems Research Institute
ASCII	American Standard Code for Information Interchange
UCAR	University Corporation for Atmospheric Research
NCAR	National Center of Atmospheric Research
NCL	NCAR Command Language
SV	Spectral variance
CCB	Cold conveyor belt
WRF	Weather Research and Forecasting
PDF	Probability density function
RMW	Radius of maximum wind
SLD	Shear layer depth

 doi:10.20944/preprints202510.1610.v1

References

1. Kuettner, J. (1959), The band structure of the atmosphere, *Tellus*, 11:3, 267-294, doi:10.3402/tellusa.v11i3.9319.
2. Walter, B. A., and J. E. Overland (1984), Observations of longitudinal rolls in a near neutral atmosphere. *Mon. Wea. Rev*., 112, 200–208.
3. Kelly, R. D. (1984), Horizontal roll and boundary-layer interrelationships observed over Lake Michigan. *J. Atmos. Sci*., **41**, 1816–1826.
4. Christian, T. W., and R. M. Wakimoto (1989), The relationship between radar reflectivities and clouds associated with horizontal roll convection on 8 August 1982. *Mon. Wea. Rev*., 117, 1530–1544.
5. Etling, D., and R.A. Brown (1993), Roll vortices in the planetary boundary layer: A review. *Boundary-Layer Meteorol*., 65, 215–248. doi:10.1007/BF00705527.
6. Young, G. S., D. A. R. Kristovich, M. R. Hjelmfelt, and R. C. Foster (2002), Rolls, streets, waves, and more: A review of quasi-two-dimensional structures in the atmospheric boundary layer. *Bull. Amer. Meteor. Soc*., 83, 997–1002, doi:10.1175/1520-0477(2002)083.
7. Wurman, J., and J. Winslow (1998), Intense sub-kilometer-scale boundary layer rolls observed in Hurricane Fran. *Science*, 280, 555-557. doi:10.1126/science.280.5363.555.
8. Gall, R., J. Tuttle, and P. Hildebrand (1998), Small-scale spiral bands observed in Hurricanes Andrew, Hugo, and Erin. *Mon. Wea. Rev*., 126, 1749–1766.
9. Ellis, R., and S. Businger (2010), Helical circulations in the typhoon boundary layer. J. Geophys. Res., 115, D06205.
10. Morrison, I., S. Businger, F. Marks, P. Dodge, and J. A. Businger (2005), An observational case for the prevalence of roll vortices in the hurricane boundary layer. *J. Atmos. Sci*., 62, 2662-2673.
11. Lorsolo, S., J. L. Schroeder, P. Dodge, and F. Marks Jr. (2008), An observational study of hurricane boundary layer small-scale coherent structures. *Mon. Wea. Rev*., 136, 2871–2893.
12. Zhang, J. A., K. B. Katsaros, P. G. Black, S. Lehner, J. R. French, and W. M. Drennan (2008), Effects of roll vortices on turbulent fluxes in the hurricane boundary layer. *Boundary-Layer Meteorol*., 128,173–189. doi:10.1007/s10546-008-9281-2.
13. Foster, R. C. (2013), Signature of large aspect ratio vortices in synthetic aperture radar images of tropical cyclones. *Oceanography*, 26, 58-67.
14. Tang, J., J. A. Zhang, P. Chan, K. Hon, X. Lei1, and Y. Wang (2021), A direct aircraft observation of helical rolls in the tropical cyclone boundary layer. *Scientific Reports*, 11, 18771. doi:10.1038/s41598-021-97766-7.
15. Schiavone, J.A., Gao, K., Robinson, D.A., Johnsen, P.J., Gerbush, M.R. (2021), Large roll vortices exhibited by Post-tropical Cyclone Sandy during landfall. *Atmosphere*, 12, 259. doi:10.3390/atmos12020259.
16. Pantillon, F., B. Adler, U. Corsmeier, P. Knippertz, A. Wieser, and A. Hansen (2020), Formation of wind gusts in an extratropical cyclone in light of Doppler lidar observations and large-eddy simulations. *Mon. Wea. Rev*., 148, 353–375. doi:10.1175/MWR-D-19-0241.1.
17. Gao, K., Ginis, I., Doyle, J. D., & Jin, Y. (2017). Effect of boundary layer roll vortices on the development of an axisymmetric tropical cyclone. *Journal of the Atmospheric Sciences*, *74*(9), 2737-2759.
18. Gao, K., & Ginis, I. (2016). On the equilibrium-state roll vortices and their effects in the hurricane boundary layer. *Journal of the Atmospheric Sciences*, *73*(3), 1205-1222.
19. Zhu, P. (2008), Simulation and parameterization of the turbulent transport in the hurricane boundary layer by large eddies, *J. Geophys. Res*., 113, D17104, doi:10.1029/2007JD009643.
20. Wang, S., and Q. Jiang (2017), Impact of vertical wind shear on roll structure in idealized hurricane boundary layers. *Atmos. Chem. Phys*., 17, 3507–3524.
21. Ito, J., T. Oizumi, and H. Niino (2017), Near-surface coherent structures explored by large eddy simulation of entire tropical cyclones. *Sci Rep* 7, 3798. doi:10.1038/s41598-017-03848.
22. Mourad, P. D., and R. A. Brown (1990), Multiscale large eddy states in weakly stratified planetary boundary layers. *J. Atmos. Sci.*, **47**, 414–438, doi:10.1175/1520-0469(1990)047<0414:MLESIW>2.0.CO;2.
23. Foster, R. C. (2005), Why rolls are prevalent in the hurricane boundary layer. *J. Atmos. Sci*., 62, 2647-2661.
24. Nolan, D. S. (2005), Instabilities in hurricane-like boundary layers, *Dynamics of Atmos. and Oceans*, 40, 209-236. doi:10.1016/j.dynatmoce.2005.03.002.

25. Nakanishi, M., and H. Niino (2012), Large-eddy simulation of roll vortices in a hurricane boundary layer. *J. Atmos. Sci*., 69, 3558–3575. doi:10.1175/JAS-D-11-0237.1.
26. Green, B. W., and F. Zhang (2015), Idealized large-eddy simulations of a tropical cyclone–like boundary layer. *J. Atmos. Sci*., 72, 1743–1764. doi:10.1175/JAS-D-14-0244.1.
27. Li, X., Z. Pu, and Z. Gao (2021), Effects of roll vortices on the evolution of Hurricane Harvey during landfall. *J. Atmos. Sci*., 78, 1847-1867. doi:10.1175/JAS-D-20-0270.1.
28. Momen, M., M. B. Parlange, and M. G. Giometto (2021). Scrambling and reorientation of classical atmospheric boundary layer turbulence in hurricane winds. *Geophysical Res. Lett*., 48, e2020GL091695. doi:10.1029/2020GL091695.
29. Gao, K., and I. Ginis (2014), On the generation of roll vortices due to the inflection point instability of the hurricane boundary layer flow. *J. Atmos. Sci*., 71, 4292–4307. doi:10.1175/JAS-D-13-0362.1.
30. Gao, K., and I. Ginis (2018), On the characteristics of linear-phase roll vortices under a moving hurricane boundary layer. *J. Atmos. Sci*., 75, 2589–2598. doi:10.1175/JAS-D-17-0363.1.
31. Katsaros, K. B., Vachon, P. W., Black, P. G., Dodge, P. P., & Uhlhorn, E. W. (2000). Wind fields from SAR: Could they improve our understanding of storm dynamics? *Johns Hopkins APL Technical Digest*, 21(1), 86-93.
32. Huang, L., Li, X., Liu, B., Zhang, J. A., Shen, D., Zhang, Z., & Yu, W. (2018). Tropical cyclone boundary layer rolls in synthetic aperture radar imagery. *Journal of Geophysical Research: Oceans*, *123*(4), 2981-2996.
33. Reppucci, A., Lehner, S., & Schulz-Stellenfleth, J. (2007, April). Tropical Cyclones Features Inferred from SAR Images. In *ENVISAT Symposium 2007* (No. 2P1, pp. 1-6).
34. NOAA National Weather Service (NWS) Radar Operations Center (1991), NOAA Next Generation Radar (NEXRAD) Level 2 Base Data. Products N0U, N0Q. NOAA National Centers for Environmental Information. https://www.ncei.noaa.gov/nexradinv/. Accessed 18 June, 2019.
35. Halverson, J. B., & Rabenhorst, T. (2013). Hurricane Sandy: The science and impacts of a superstorm. *Weatherwise*, *66*(2), 14-23.
36. Comes, T., & Van de Walle, B. A. (2014). Measuring disaster resilience: The impact of Hurricane Sandy on critical infrastructure systems. *ISCRAM*, 11(May), 195-204.
37. Mattingly, K. S., McLeod, J. T., Knox, J. A., Shepherd, J. M., & Mote, T. L. (2015). A climatological assessment of Greenland blocking conditions associated with the track of Hurricane Sandy and historical North Atlantic hurricanes. *International Journal of Climatology*, *35*(5).
38. Qian, W. H., Huang, J., & Du, J. (2016). Examination of Hurricane Sandy's (2012) structure and intensity evolution from full-field and anomaly-field analyses. *Tellus A: Dynamic Meteorology and Oceanography*, 68(1), 29029.
39. Shin, J. H. (2019). Vortex spinup process in the extratropical transition of Hurricane Sandy (2012). *Journal of the Atmospheric Sciences*, *76*(11), 3589-3610.
40. Galarneau Jr, T. J., Davis, C. A., & Shapiro, M. A. (2013). Intensification of Hurricane Sandy (2012) through extratropical warm core seclusion. *Monthly Weather Review*, *141*(12), 4296-4321.
41. Martínez, P., Pérez, I. A., Sánchez, M. L., García, M. D. L. Á., & Pardo, N. (2021). Wind Speed Analysis of Hurricane Sandy. *Atmosphere*, *12*(11), 1480.
42. Zhu, T., & Weng, F. (2013). Hurricane Sandy warm-core structure observed from advanced Technology Microwave Sounder. *Geophysical Research Letters*, 40(12), 3325-3330.
43. Shin, J. H., & Zhang, D. L. (2017). The impact of moist frontogenesis and tropopause undulation on the intensity, size, and structural changes of Hurricane Sandy (2012). *Journal of the Atmospheric Sciences*, 74(3), 893-913.
44. Kowaleski, A. M., & Evans, J. L. (2018). Relationship between the track and structural evolution of Hurricane Sandy (2012) using a regional ensemble. *Monthly Weather Review*, 146(12), 4279-4302.
45. Schiavone, J. A. (2023), Airstream association of large boundary layer rolls during extratropical transition of Post-tropical Cyclone Sandy (2012). *Meteorology*, 2, 368–386. https://doi.org/10.3390/meteorology2030022.
46. Blake, E. S., T. B. Kimberlain, R. J. Berg, J. P. Cangialosi, and J. L. Beven III (2013), Tropical Cyclone Report: Hurricane Sandy (AL182012). Tech. Rep. AL182012, NOAA/National Hurricane Center, 157 pp.
47. Rutgers NJ Weather Network (2014), https://www.njweather.org/data/5min.

 doi:10.20944/preprints202510.1610.v1

48. NOAA National Data Buoy Center (2016), https://www.ndbc.noaa.gov/.
49. NOAA Weather and Climate Toolkit (2021), https://www.ncdc.noaa.gov/wct/.
50. The NCAR Command Language (Version 6.6.2) [Software]. (2019). Boulder, Colorado: UCAR/NCAR/CISL/TDD. http://dx.doi.org/10.5065/D6WD3XH5
51. Landsea, C. W. & J. L. Franklin (2013). Atlantic hurricane database uncertainty and presentation of a new database format. *Monthly Weather Review*, 141, 3576-3592.